Water-Accelerated Photo-oxidation of CH₃NH₃PbI₃ Perovskite: Mechanism, rate orders, and rate constants

Timothy D. Siegler,[†a] Wiley A. Dunlap-Shohl,[†a] Yuhuan Meng,[a] Wylie F. Kau,[a] Preetham P. Sunkari,[a] Chang En Tsai,[a] Zachary J. Armstrong,[a] Yu-chia Chen,[b,c] David A. C. Beck,[a,c] Marina Meila,[d,c] Hugh W. Hillhouse*[a]

[a] Department of Chemical Engineering, Clean Energy Institute, and Molecular Engineering and Science Institute, [b] Department of Electrical and Computer Engineering, [c] eScience Institute, [d] Department of Statistics

University of Washington, Seattle, WA, United States, 98195

* Corresponding author: h2@uw.edu
[†] These authors contributed equally

Abstract

Understanding the chemical reactions that hybrid organic-inorganic halide perovskite (HP) semiconductors undergo in the presence of moisture, oxygen, and light are essential to the commercial development of HP solar cells and optoelectronics. Here we use optical absorbance to study the kinetics of methylammonium lead iodide (MAPbI₃) degradation in response to combinations of moisture, oxygen, and illumination over a range of temperatures. We identify two primary reaction pathways that dominate MAPbI₃ material degradation in these mixed environmental conditions: (1) dry photooxidation (DPO) due to the combined role of oxygen and photoexcited electrons (with a rate of 2 x 10⁻⁹ mol/m²·s in dry air at 25 °C and an effective activation energy of 0.62 eV), and (2) a water-accelerated photooxidation (WPO) process due to the combined role of water, oxygen, and photoexcited electrons (with a rate of 1 x 10⁻⁷ mol/m²s in 50% RH air at 25 °C and observed effective activation energy of 0.07 eV). Commonly reported humidity-only, blue light, and thermal degradation pathways are demonstrated to have rates that are respectively 100, 1000, and >1000 times slower than predominant photooxidation processes in ambient conditions. Extracting kinetic rate constants from the dynamics of the initial degradation, we calculate that in dry air, photooxidation rate of MAPbI₃ follows a $f(x) \propto x/(1 + Kx)$ relationship with respect to oxygen in the vapor phase (P_{O2}) and excess concentration of photoexcited electrons (n). In humid air, photooxidation of MAPbI₃ exhibits first order kinetics with respect to the partial pressure of water in the vapor phase (P_{H2O}). However, with respect to P_{O2} and n, kinetics follow a $f(x) \propto x/(1 + kx)^2$ relationship with respect to rate. We then identify a plausible reaction mechanism for degradation of MAPbI₃ material that is consistent with these rate functionalities. The rate determining step for both DPO and WPO is proton abstraction by photogenerated superoxide radicals. However, proton donation by adsorbed water proceeds much more rapidly than donation by methylammonium, resulting in faster degradation rates for WPO at typical ambient conditions (~50% RH). Rate laws derived from this mechanism were fit to the entire dataset to extract rate constants for DPO and WPO processes. Accurate predictions of material degradation rates, with narrow confidence intervals of fit parameters as identified by the Bootstrap algorithm, provide the first experimental estimates of the equilibrium constants of oxygen adsorption on MAPbI₃ ($K_{eq} \approx 3$ x 10^{-3} kPa⁻¹) and superoxide generation from adsorbed oxygen and photoexcited electrons in MAPbI₃ ($K_{eq} \approx 5$ x 10^{-15} (photons/m²·s)⁻⁰·⁷). Given that water has been reported as a degradation product of DPO, the results reported here highlight the need for the development of encapsulation schemes that rigorously block oxygen, as over longer time

periods, product water (if generated) may accumulate inside the packaging and initiate the much faster WPO process.
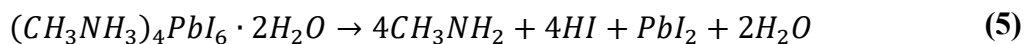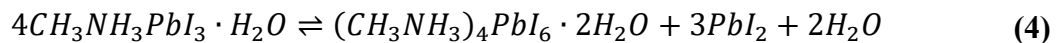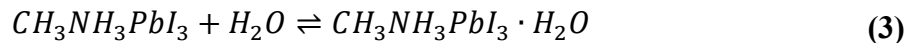
Introduction

Halide perovskite (HP) photovoltaics (PVs) are the first printable photovoltaic technology to achieve >25% power conversion efficiency (PCE),[1] which may allow for low-cost high-efficiency flexible PV devices fabricated by roll-to-roll printing technology.[2,3] Given the low cost of the starting materials, rigid devices such as perovskite-silicon tandems[4,5] or devices formed by vapor deposition could also lead to significant decreases in the cost of solar power if the solar cells have sufficiently long service lifetime. While a large number of studies have identified HP PV devices with >1,000 hr operational lifetimes,[6–10] a U.S. Department of Energy analysis indicates that solar panels will need >30 yr service lifetimes with year-over-year degradation rates of less than 0.5% for a panel to reach $0.03/kWh levelized cost of energy (assuming a 20% total-area efficiency and a module cost of $0.19/$W_p$).[11] Testing the stability of any technology on multi-decade timescales is impractical. Therefore, warranties backing the long-term performance of HP-based commercial products will necessarily rely on predictions of service lifetime. While accelerated aging tests like the IEC 61215 standard (which includes testing the drop in performance after the panel is held at 85 °C and 85% RH for 1,000 hrs)[12] have been used to estimate service lifetime and provide performance guarantees,[7,8] these tests have only been validated for silicon and thin film based PV technologies like CdTe.[13–15] Unlike in Si or CdTe, HPs break down due to chemical reactions of the semiconductor with water, oxygen, and photoexcited electrons,[6,16–20] and there exists a strong correlation between decay of optoelectronic properties such as carrier diffusion length and material transformation rate.[21,22] In oxygen and light, a photooxidation-induced degradation of MAPbI3 has been reported previously[19,23,24] and is widely believed to occur via a mechanism that involves superoxide radical ($O_2^{\bullet-}$) generated by photoexcited electrons in the conduction band of MAPbI3 to yield the overall reaction:[18–20,23,24]

$$4CH_3NH_3PbI_3 + O_2 + h\nu \rightarrow 4PbI_2 + 4CH_3NH_2 + 2H_2O + 2I_2 \tag{1}$$
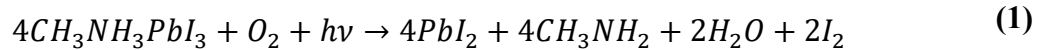
Others have disputed the generation of water in this process, citing instead the overall reaction[20,25] (note that PbI2 and I2 are not directly reported in [20] or [25], but necessarily must be formed as stated to maintain charge and species conservation through the reaction):

$$CH_3NH_3PbI_3 + O_2 + h\nu \rightarrow CH_3NH_2 + O_2 + \frac{1}{2}H_2 + PbI_2 + \frac{1}{2}I_2 \tag{2}$$
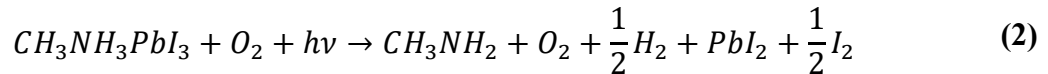
In humid environments, attack by moisture is widely reported to be the primary mode of degradation in MAPbI3 thin films,[16,17] with a reported degradation pathway of:

$$CH_3NH_3PbI_3 + H_2O \rightleftharpoons CH_3NH_3PbI_3 \cdot H_2O \tag{3}$$

$$4CH_3NH_3PbI_3 \cdot H_2O \rightleftharpoons (CH_3NH_3)_4PbI_6 \cdot 2H_2O + 3PbI_2 + 2H_2O \tag{4}$$

$$(CH_3NH_3)_4PbI_6 \cdot 2H_2O \rightarrow 4CH_3NH_2 + 4HI + PbI_2 + 2H_2O \tag{5}$$

Despite these proposed overall reactions, quantitative acceleration factors describing how increasing oxygen, humidity, or illumination levels impact HP material degradation rate are still unknown. Without knowledge of these functionalities, it is unlikely that service lifetime

predictions derived from accelerated-aging tests will be accurate. Recent machine learning studies have emerged to in an attempt to fill this predictive gap,[21,26–28] with ML models identifying material decomposition rate (rate of increase of transmittance) as the most important quantitative predictors of diffusion length degradation over time (diffusion length T80).[21] However, if these models are to be predictive over multi-decade time scales, understanding of the physics that that govern MAPbI$_3$ degradation are required. Given the strong correlation between HP material degradation and that of their optoelectronic performance, accurate prediction of HP device lifetimes will greatly benefit from a fundamental understanding of the degradation mechanisms and the kinetics of each pathway of material degradation.

The degradation mechanisms and rates for commercial optoelectronics have been well-studied. For example, light-induced degradation due to the Staebler-Wronski effect in amorphous silicon has an understood mechanism and rate orders,[29] and the light-induced degradation in crystalline silicon PVs has been demonstrated to be due to oxidation of boron defects in the silicon lattice, with well-agreed upon activation energies and rate constants for both slow and fast boron deactivation processes.[14] Despite the importance of HP degradation reactions, a formal mechanism with rate orders and rate constants has not been reported. Some reports of effective rate constants and activation energies of perovskite degradation exist from fits to either inverse degradation times[30] or an Avrami model[31] based on the time-evolution of optical absorbance,[32] XRD patterns,[33–36] XPS peaks,[37] and AFM features of degrading HP films.[38] However, quantitative relationships between the rate of perovskite degradation and ambient partial pressure of oxygen, the illumination intensity, and the partial pressure of water vapor are still unknown.

Here, we measure the kinetics of methylammonium lead iodide (MAPbI$_3$) perovskite transformation using changes in optical transmittance measured in-situ as a function of humidity, oxygen, illumination intensity, and temperature to construct a rate law equation. Transmittance is collected with an incident photon wavelength of 550 nm (~2.25 eV), which is above the bandgap of MAPbI$_3$ (1.6 eV) and below the bandgap of all reported solid degradation products, namely: PbI$_2$ (2.35 eV),[16,39] CH$_3$NH$_3$PbI$_3$·H$_2$O (3.1 eV),[32] CH$_3$NH$_3$PbI$_3$·2H$_2$O (3.9 eV),[40] and PbO$_{1-x}$(OH)$_{2x}$ (>2.5 eV).[41] Increases in transmittance are therefore interpreted as conversion of MAPbI$_3$ to degradation products. Similar approaches were recently taken to identify thermal degradation rates in various perovskites,[30,42] where the reciprocal of the time to 80% of initial absorbance T80 was taken as a simple "rate constant" with units of s^{-1}. Here, we use transmittance measurements to rigorously calculate the initial MAPbI$_3$ consumption rate (r_{MAPI}) in mol·m^{-2}·s^{-1}. We identify and quantify two mechanisms of degradation: (a) a dry photooxidation (DPO) process that occurs in the absence of vapor-phase water, and (b) a water-accelerated photooxidation (WPO). For each mode of degradation, we identify how varying environmental conditions impact r_{MAPI} in both regimes, extracting effective activation energies and rate orders in humidity, oxygen, and light. The experimentally determined rate orders are highly suggestive of certain elementary steps in the mechanism, and we propose a detailed reaction mechanism for the degradation for MAPbI$_3$ in the presence of oxygen, light, and humidity that explains the functionality of the rate law. The derived detailed reaction mechanism demonstrates that H$_2$O accelerates the photooxidation process of MAPbI$_3$.

Results and Discussion

The degradation of MAPbI₃ was monitored *in-situ* under controlled environmental conditions by simultaneous measurement of transmittance and quantitative photoluminescence.[21,43] (see Figure 1a). Environmental conditions are controlled using a small chamber with gas ports, a heater, and windows above and below the sample to admit incident and transmitted light. The optical transmittance ($\mathcal{T}$, ratio of the sum of direct and diffuse transmitted intensity divided by incident intensity) is measured using incident 550 ± 15 nm monochromatic light from an LED source and notch filter, with transmitted light collected by a calibrated silicon photodiode placed below the sample. Increasing $\mathcal{T}$ at 550 nm indicates increased degradation of the MAPbI₃ film (E_g = 1.6 eV, 775 nm) into PbI₂ (E_g = 2.35 eV, 525 nm) and volatile byproducts.[6,21,32] Absolute values of transmittance of a MAPbI₃ film placed the environmental chamber (which in turn is affixed to a microscope stage) are difficult to obtain *in-situ*. Measured transmittance values on the same sample may change significantly based on position and orientation of the MAPbI₃ film in the chamber, the alignment of the photodiode sensor (which must be repositioned after focusing each sample due to adjustment of the z-height of the microscope stage during experimental setup), stray light from the environment, and other uncontrolled factors. To minimize these effects, it is desirable to use the transmittance normalized by the initial transmittance, ($\mathcal{T}_t/\mathcal{T}_0 = I_t/I_0$). This is the measured data in the experiments.
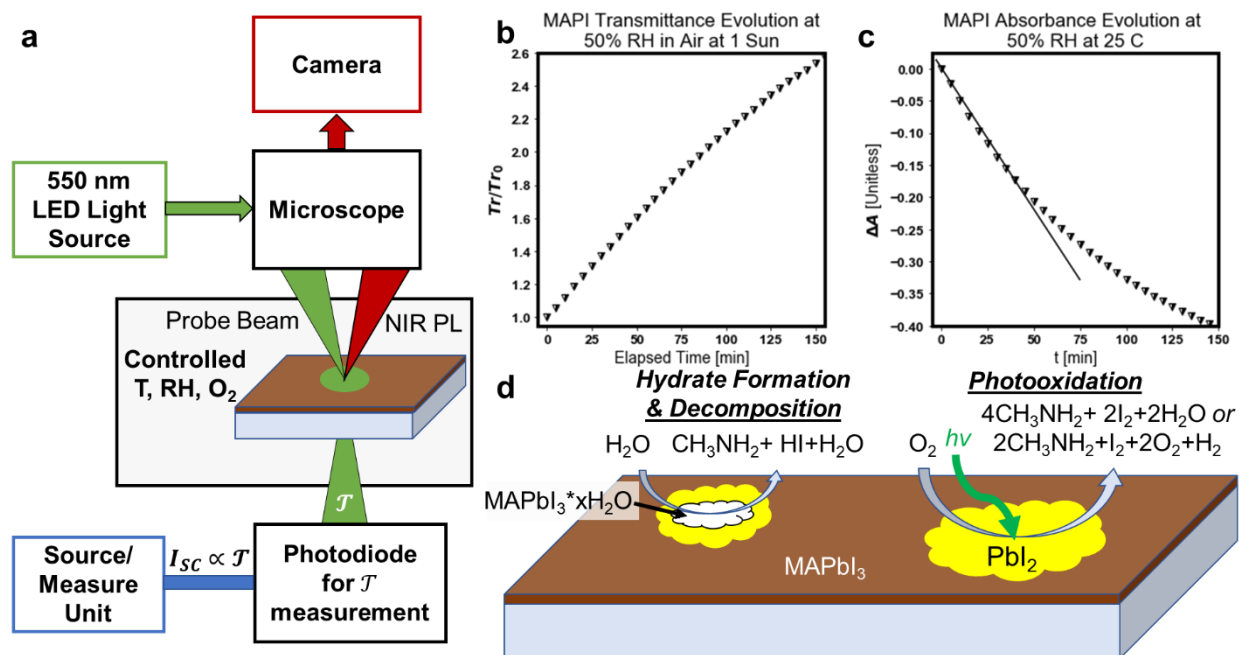

Figure 1. (a) Schematic of the experimental setup used to monitor perovskite decomposition under controlled environmental conditions. (b) Example of the evolution of transmittance for MAPbI₃ at 50% RH in air at 1 Sun effective illumination. (c) Change in absorbance over time, showing an initial linear region of a MAPbI₃ sample at 25 °C in 50% RH air under 1 Sun illumination. (d) Schematic detailing the most commonly reported degradation mechanisms of MAPbI₃ in literature: hydrate formation (requiring only water) and photooxidation (requiring only oxygen and light) with degradation products variously reported as either H_2 or H_2O.

For our purposes, the transmittance is important only in so far as it is used to calculate the absorbance, which can be related to the number of moles of perovskite (*N*). The Beer-Lambert law

related the absorbance (A) to the conventionally defined material absorption coefficient α, $A = \alpha \cdot L \cdot log_{10}(e)$. As degradation occurs, perovskite is converted to higher bandgap materials and the effective absorption coefficient (above the perovskite bandgap but below the bandgap of the products) decreases. To account for this, we define an effective absorption coefficient, $\alpha = \alpha_0 \cdot (N/N_0)$ where α_0 is the absorption coefficient of pristine perovskite at the wavelength of the incident light (550 nm) and N_0 is the initial number of moles of $CH_3NH_3PbI_3$ in the beam path. Substituting in the effective absorption coefficient and taking the derivative with respect to time yields, $dA/dt = \alpha_0 \cdot (1/N_0) \cdot L \cdot log_{10}(e) \cdot dN/dt$. In the early stages of degradation, the change in absorbance evolves linearly with time (Figure 1c) and is relatively independent of film thickness below 500 nm (Figure S3). This suggests that the degradation reaction is dominated by surface reactions and is effectively zeroth order with respect to $MAPbI_3$ (see §3 in Supporting Information). Thus, the rate of disappearance of $MAPbI_3$ is defined as negative the rate of change of moles of $MAPbI_3$ per unit area (W) of the illuminated film, $r_{MAPI} = -(1/W) \cdot dN/dt$. Plugging in the relation above between dA/dt and dN/dt and using $N_0/(W \cdot L) = \rho/M$, where ρ is the density of pristine perovskite and M is the formula weight, the equation for the rate of disappearance of perovskite in terms of absorbance is:

$$r_{MAPI} = -\frac{1}{W}\frac{dN}{dt} = -\frac{\rho}{M \cdot log_{10}(e) \cdot \alpha_0}\frac{dA}{dt} \qquad (6)$$

When changes in reflectance are small relative to changes transmittance, the rate of change of absorbance may be well approximated from transmittance measurements only. For the case where reflectance (both specular and diffuse) is dominated by the front interface reflectivity, the absorbance is $A = -log_{10}(\mathcal{T}/(1-R))$. Conveniently, the difference between the absorbance at time t minus the initial absorbance, ΔA, can be calculated directly from the measured transmittance normalized to time-zero values ($\mathcal{T}_t/\mathcal{T}_o$):

$$\Delta A = A_t - A_o = -log_{10}\left(\frac{\mathcal{T}_t}{1-R_t}\right) - \left(-log_{10}\left(\frac{\mathcal{T}_o}{1-R_o}\right)\right) \qquad (7)$$

$$\Delta A = -log_{10}\left(\frac{\mathcal{T}_t}{\mathcal{T}_o}\right) - log_{10}\left(\frac{1-R_o}{1-R_t}\right) \qquad (8)$$

For the films measured here at early stages of degradation, and with the probe wavelength of 550 nm, $(1-R_o)/(1-R_t)$ approaches 1, and thus the second term approaches zero, yielding:

$$\Delta A \approx -log_{10}\left(\frac{\mathcal{T}_t}{\mathcal{T}_o}\right) = -log_{10}\left(\frac{I_t}{I_o}\right) \qquad (9)$$

Also, $d(\Delta A)/dt = dA/dt$. The reflectance does change a little with time, and we directly measure the error in the rate of reaction associated with neglecting the changes in reflectance to be 1% at 550 nm (see section 2 and Figure S1 of the Supporting Information). Depending on how the incident wavelength aligns with the maxima or minima of the reflectance (which depends on film thickness), the error can be larger (see Figure S1) and should be estimated for other experimental situations. Given that the film thickness is effectively constant in the data set reported here, 260 nm ± 10 nm, the systemic error is small. Further, given that the differences in the rate of reaction presented below span 3 orders of magnitude, the error associated with neglecting changes in reflectance does not affect any of the conclusions below.

The rate of change of absorbance encodes the dynamics of the MAPbI$_3$ degradation reaction and is a function of (at least) temperature, humidity, oxygen, and illumination intensity. Note that other factors may affect the rate as well like grain size and the concentration of point defects. Smaller grain sizes increase the grain boundary surface area and should increase the observed rate. With regard to defects, iodide vacancies in particular have been shown to facilitate superoxide formation and should also increase the observed rate.[44] The initial rate of degradation was determined using linear fits of the change in absorbance and Equation 6 at a variety of environmental conditions (Figure 2a-d and Table 1), both in the dark and under 1 Sun illumination (which here for a 1.6 eV bandgap material is approximated by continuous illumination with 1.59 x 10^{21} above-bandgap-photons·m^{-2}·s^{-1}). The initial rates reveal that photo-induced degradation in the presence of oxygen is faster than any process without oxygen (dry thermal or humid thermal under illumination or in the dark) by more than an order of magnitude at both 25 °C and 85 °C. Dry oxygen and humid oxygen pathways are approximately equal at 85 °C, while the humid-oxygen pathway dominates at 25 °C by almost two orders of magnitude. Importantly, the data show that in the absence of oxygen, humidity-only degradation is much slower relative to degradation in the presence of oxygen. Similarly, other reported degradation pathways that contribute to MAPbI$_3$ degradation are much also much slower than photooxidation processes. Thermal degradation[45] at 85 °C is three orders of magnitude slower than photooxidative degradation. C-N bond cleavage in methylammonium due to blue light (λ>410 nm) exposure has also been reported to contribute to MAPbI$_3$ degradation.[20,25] However, exposure to 1 sun equivalent of 395 nm light results in degradation rates below 1 x 10^{-11} mol/m^{2}s, again over three orders of magnitude slower than photooxidation processes. A summary of relative rates of degradation is shown in Table 1.

The temperature dependences of photooxidation in both dry and humid air are well-fit by Arrhenius relationships, with observed effective activation energies of $E_{\text{DPO}}^{\text{eff}} = 0.62$ eV in dry air (rate due to DPO only) and $E_{\text{DPO+WPO}}^{\text{eff}} = 0.07$ eV in 50% RH air (the observed rate, representing the sum of DPO and WPO). Note that these values do not necessarily correspond to the true activation energy of a single reaction step alone, but may be convoluted with characteristic energies of other processes like species adsorption (discussed below). As a result of this dramatic difference, photooxidation rates in the presence and absence of humidity differ significantly depending on the temperature, and dry photooxidation proceeds at a rate that is over an order of magnitude slower than humidity-assisted photooxidation at 25 °C (Table 1). Together these results indicate that water and oxygen synergistically accelerate MAPbI$_3$ degradation. It is sometimes assumed that the observed increased degradation rate in the presence of both oxygen and water is due to the additive effects of humidity only (degradation via hydrate formation) and dry photooxidative pathways.[46] However, degradation rates in humidity without oxygen and in oxygen without humidity both proceed at over an order of magnitude slower pace than MAPbI$_3$ degradation rate in the presence of both humidity and oxygen. These data thus point to water acting as an accelerant (technically not a catalyst since water is consumed as an intermediate and then generated as a product) for photooxidation of MAPbI$_3$, rather than contributing to degradation via a parallel hydration pathway.

This behavior is consistent with some speculation in literature. Aristidou et. al. have reported that exposing MAPbI$_3$ films to humid N$_2$ prior to degradation in dry air increases the photooxidation rate.[23] They speculate that this acceleration is due to increasing proton concentration at the MAPbI$_3$ surface, enhancing the chemical driving force for superoxide

protonation.[23] Figure 2 corroborates the experimental observations of Aristidou et al.,[23] demonstrating that the presence of humidity dramatically increases photooxidation rate, even in the vapor phase. However, data in Figure 2 demonstrates that the presence of water does not merely provide additional protons to contribute to reaction, but that water creates a different lower energy barrier pathway for the overall reaction.
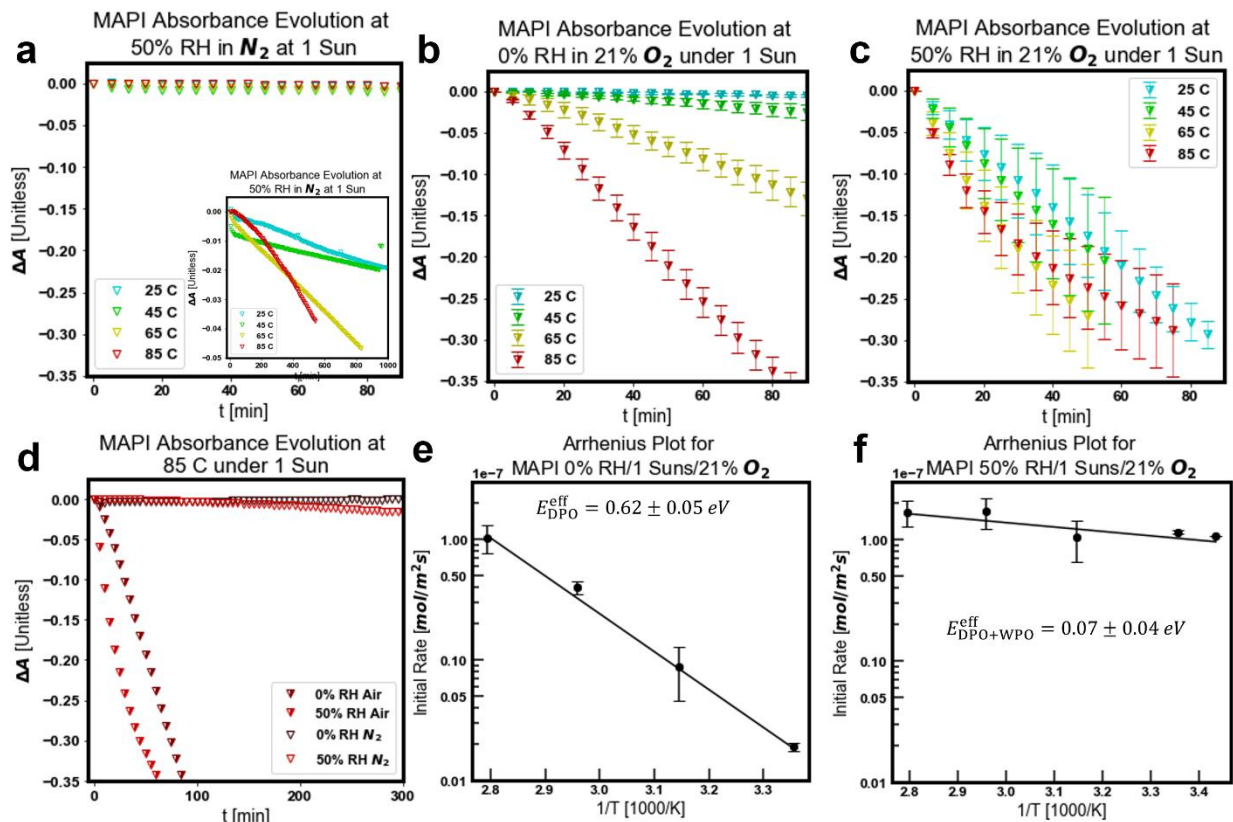

Figure 2. Absorbance evolution of MAPbI$_3$ thin films vs time aged at 25, 45, 65, and 85 $^\circ$C under 1 sun excitation in (a) 50% RH N$_2$, (b) 0% RH air ("dry air"), and (c) 50% RH air ("humid air"). (d) Degradation proceeds rapidly in both humid and dry air, but slowly in humid and dry nitrogen, indicating that the primary modes of MAPbI$_3$ degradation are photooxidation and humidity-accelerated photooxidation. Arrhenius plots of initial MAPbI$_3$ degradation in (e) dry and (f) humid air conditions.

Table 1. Upper bounds on degradation rates of different degradation processes at 25 and 85 °C. While the initial degradation rate for photooxidation at 85 °C in both dry and humid air is ~10^{-7} mol/m^2/s, degradation in humid nitrogen is 2 orders of magnitude lower, and degradation due to thermal-only and light-only degradation processes in inert environments is over 3 orders of magnitude slower than photooxidative processes. The full table showing degradation in corresponding dark conditions is in Supporting Information as Table S2. In most cases, degradation in the dark is dominated by the periods during which the sample is illuminated by the probe beam when collecting optical measurements, as seen by the acceleration of degradation when the measurement frequency is increased (see §4 of Supporting Information). Where repeat runs were performed, the uncertainty is represented by the standard deviation ($\pm\sigma$). The random error associated with sample-to-sample variation in the degradation rate is <30% in all cases reported here and is of similar scale to the upper bound on the systematic error associated with neglecting reflectance effects (see §2 of Supporting Information and Figure S1). At a probe wavelength of 550 nm, however, the systematic error is much lower (~1%) and is therefore generally insignificant relative to sample-to-sample variation.

Degradation Conditions	25 ºC with 1 Sun [mol/(m^2·s)]	85 ºC with 1 Sun [mol/(m^2·s)]
Heat Only (0% O$_2$, 0% RH)	less than 10^{-11}	less than 10^{-11}
Humid N$_2$ (0% O$_2$, 50% RH)	1×10^{-9}	3×10^{-9}
Dry Air (21% O$_2$, 0% RH)	$2 \pm 0.2 \times 10^{-9}$	$1 \pm 0.3 \times 10^{-7}$
Humid Air (21% O$_2$, 50% RH)	$1 \pm 0.1 \times 10^{-7}$	$2 \pm 0.6 \times 10^{-7}$

Having identified primary degradation modes, rate orders in humid and dry air conditions are determined by establishing a baseline set of conditions for dry photooxidation (85 ºC, 0% RH, 21 kPa O$_2$, 1 sun illumination after >2 hr annealing at 100 ºC in dry N$_2$ to drive off residual water or solvent) and humid photooxidation (25 ºC, 50% RH, 21 kPa O$_2$, 1 sun illumination) degradation modes and measuring the response of sample absorbance to varying oxygen content, illumination intensity, and (where relevant) humidity levels. Results are shown in Figure 3. In humid air, the rate of MAPbI$_3$ degradation (r_{MAPI}) proceeds with rate orders of 1.3 ± 0.3 (i.e., approximately first order) with respect to the partial pressure of water in the gas phase, 0.28 ± 0.05 with respect to the partial pressure of oxygen, and 0.25 ± 0.03 with respect to the illumination intensity. In dry air, r_{MAPI} proceeds with rate orders of 0.70 ± 0.15 with respect to oxygen, and 0.27 ± 0.03 with respect to illumination intensity. The rate of reaction does not depend on illumination intensity directly, but incident photons create excess electrons and holes that do undergo reactions. The relationship between illumination intensity and excess electron concentration is determined from the relationship between illumination intensity and photoconductivity[43,47] (which linearly depends on excess carrier concentration) which for MAPbI$_3$ thin films, has been determined to be a power law relation between n $\propto$ N$_{suns}^{0.4}$ and N$_{suns}^{0.73}$. These results are consistent with our samples, which show n $\propto$ N$_{suns}^{0.67}$ (Figure S5, §5 in Supporting Information). We use n $\propto$ N$_{suns}^{0.7}$ to fit rate expressions in terms of n throughout this report.

Experimentally determined rate orders constrain the possible reaction mechanisms. If the elementary steps are known (or can be guessed by physicochemical reasoning) and the rate of one step determines the rate of the overall reaction (while all other steps are in quasi-equilibrium), then an approximate rate equation can be derived. While the concept of a rate determining step (RDS) is often debated[48,49] with compelling reasons to develop more general approaches, the approach

has tremendous utility in deriving the functional form of approximate rate equations for many multi-step reactions.[50,51]
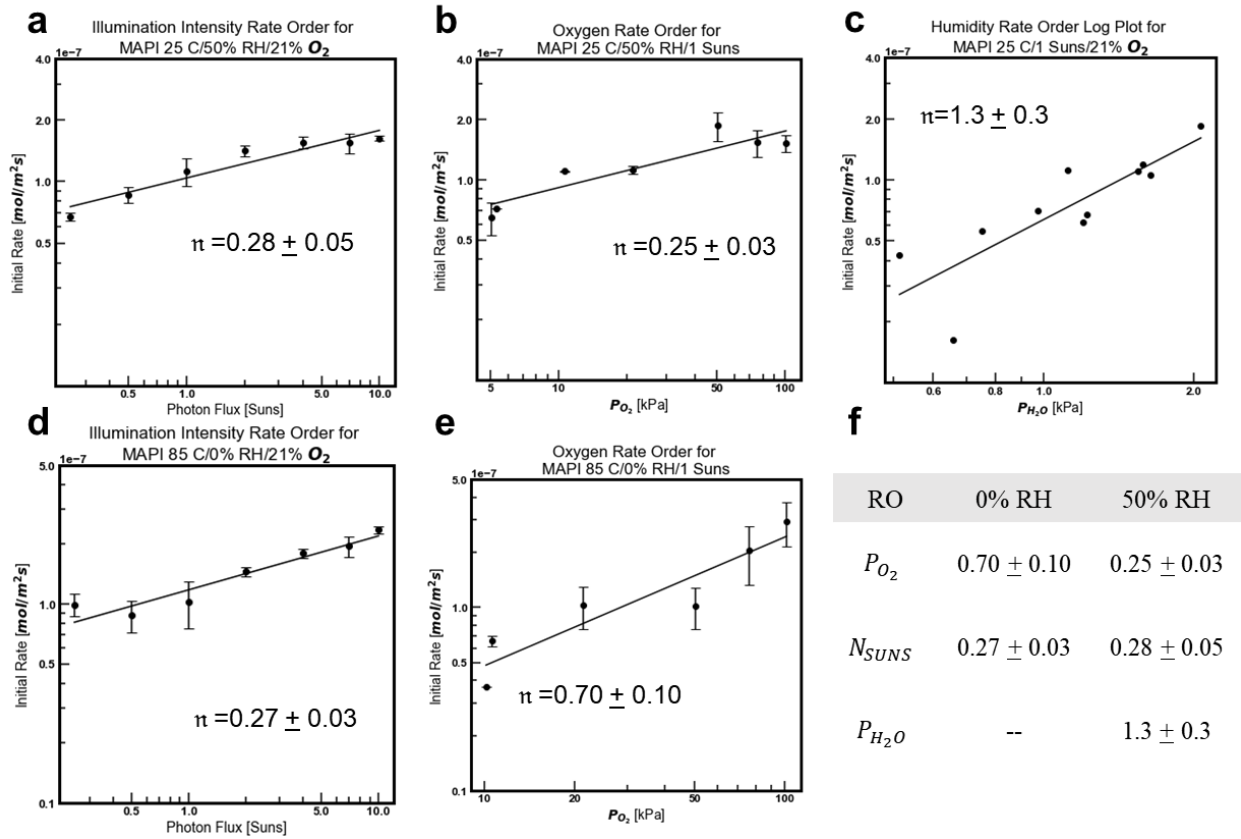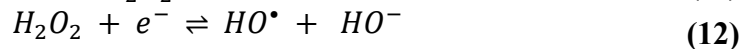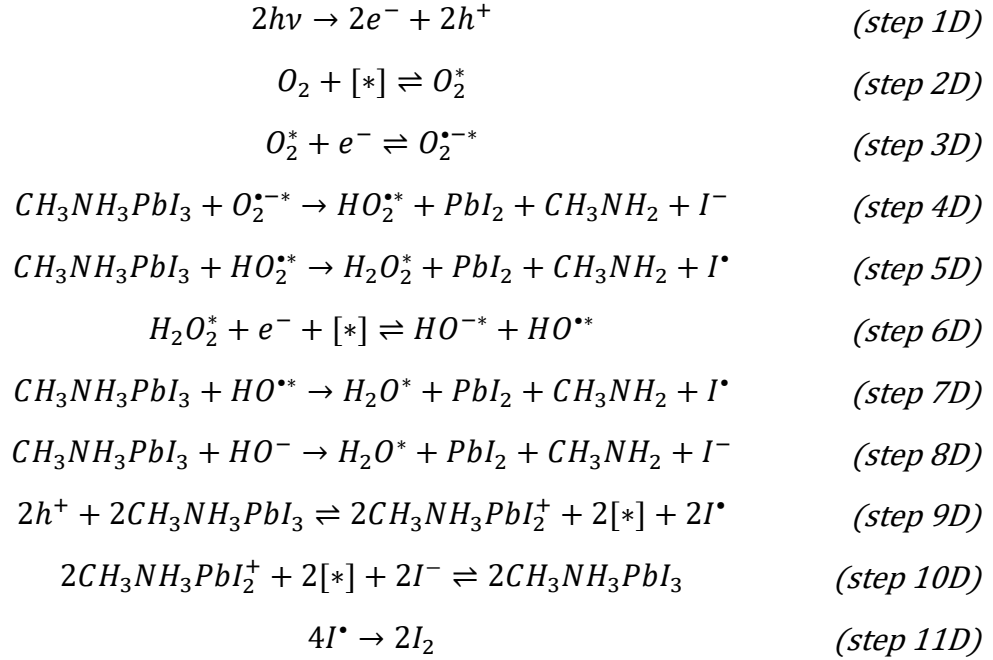

Figure 3. Effective rate orders based on initial degradation rates for (a) illumination, (b) oxygen, and (c) water for MAPbI$_3$ films at 25 °C in humid atmospheres and (d) illumination and (e) oxygen at 85 °C in dry atmospheres. (f) A summary table of effective rate orders in oxygen, illumination, and moisture.

Considering possible pathways for photooxidation (without water), previously it has been reported that neutral oxygen adsorbs on the surface of MAPbI$_3$ (preferably in/on iodide vacancies)[19,52] in an unoccupied adsorption site ([*]) and then gets reduced by photoexcited electrons from the conduction band of MAPbI$_3$ to form superoxide radical, ($O_2^{\bullet-}$).[24,41,52] Further, it has been reported[18,20,53] that superoxide radicals abstract a proton from the methylammonium cation (CH$_3$NH$_3^+$). Such a mechanism would yield an adsorbed hydroperoxyl radical ($O_2^{\bullet-*}$ + $H^+ \rightarrow HO_2^{\bullet*}$).[54] Once this species is present, other reactive oxygen species (ROS) are possible, including but not limited to:

$$2\ HO_2^{\bullet} \ \rightleftharpoons\ H_2O_2\ +\ O_2 \tag{10}$$
$$H_2O_2 \rightleftharpoons\ 2HO^{\bullet} \tag{11}$$
$$H_2O_2\ +\ e^-\ \rightleftharpoons HO^{\bullet}\ +\ HO^- \tag{12}$$

Each of the reactive oxygen species $(O_2{}^{\bullet-}, HO_2{}^{\bullet}, H_2O_2, HO^{\bullet}, HO^{-})$ may react with methylammonium, abstracting either a proton or a neutral hydrogen. One ***plausible*** complete dry photo-oxidation pathway is shown in scheme 1.

Scheme 1. One Plausible Dry photo-oxidation Pathway. Primary degradation mechanism of MAPbI₃ in the absence of water but in the presence of oxygen, above bandgap incident photons, and surface adsorption sites [*].

$$2h\nu \rightarrow 2e^- + 2h^+ \qquad \text{(step 1D)}$$

$$O_2 + [*] \rightleftharpoons O_2^* \qquad \text{(step 2D)}$$

$$O_2^* + e^- \rightleftharpoons O_2^{\bullet-*} \qquad \text{(step 3D)}$$

$$CH_3NH_3PbI_3 + O_2^{\bullet-*} \rightarrow HO_2^{\bullet*} + PbI_2 + CH_3NH_2 + I^- \qquad \text{(step 4D)}$$

$$CH_3NH_3PbI_3 + HO_2^{\bullet*} \rightarrow H_2O_2^* + PbI_2 + CH_3NH_2 + I^{\bullet} \qquad \text{(step 5D)}$$

$$H_2O_2^* + e^- + [*] \rightleftharpoons HO^{-*} + HO^{\bullet*} \qquad \text{(step 6D)}$$

$$CH_3NH_3PbI_3 + HO^{\bullet*} \rightarrow H_2O^* + PbI_2 + CH_3NH_2 + I^{\bullet} \qquad \text{(step 7D)}$$

$$CH_3NH_3PbI_3 + HO^- \rightarrow H_2O^* + PbI_2 + CH_3NH_2 + I^- \qquad \text{(step 8D)}$$

$$2h^+ + 2CH_3NH_3PbI_3 \rightleftharpoons 2CH_3NH_3PbI_2^+ + 2[*] + 2I^{\bullet} \qquad \text{(step 9D)}$$

$$2CH_3NH_3PbI_2^+ + 2[*] + 2I^- \rightleftharpoons 2CH_3NH_3PbI_3 \qquad \text{(step 10D)}$$

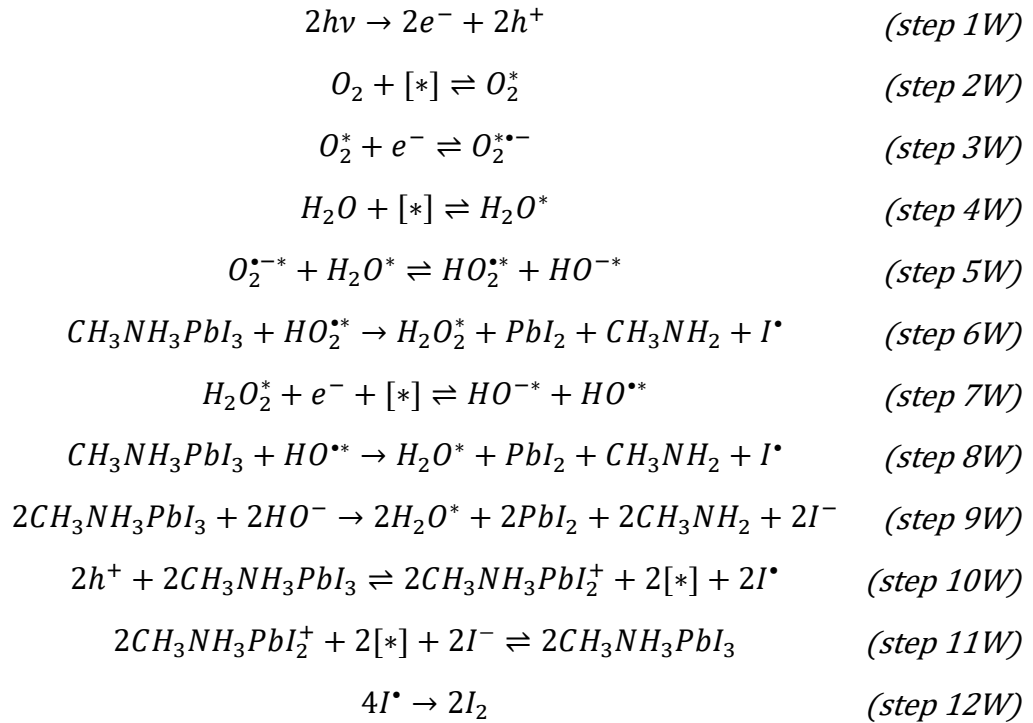$$4I^{\bullet} \rightarrow 2I_2 \qquad \text{(step 11D)}$$

There are many ways that the reaction in scheme 1 can happen from step 4D onwards, depending on the relative rates of formation of different ROS and the specific products (see §6 of Supporting Information). However, most variations result in the same rate law that is zeroth order in oxygen and first order in concentration of electrons, provided that step 4D (proton abstraction from methylammonium by superoxide) is the rate determining step. The resulting rate equation for dry photo-oxidation (DPO) degradation of MAPbI₃ is (see §6 of Supporting Information for derivations):

$$r_{DPO} = -k_{DPO} \frac{P_{O_2} n}{1 + K_{2D} P_{O_2} (1 + K_{3D} n)} \qquad \textbf{(13)}$$

where $k_{DPO} = k_{0,DPO}\, e^{-E_{A,DPO}^{\text{eff}}/k_B T}$. The measured rate of dry photo-oxidation is compared to the derived rate law in Figure 4. It is important to note that in these experiments dry air is swept over the sample, and thus any water, iodine (see §8 of Supporting Information), or other volatile products) are removed from the system. In a device architecture, especially encapsulated architectures, these products will build-up. This could be especially problematic with water since the water-accelerated photo-oxidation is much faster than dry photo-oxidation, and over time an encapsulated film may transition from dry photo-oxidation to water-accelerated photo-oxidation. Further, it suggests that oxygen barrier properties might be the most critical packaging perovskite solar cells for long-term stability.

In the presence of water, many additional pathways are possible to form ROS. One reaction that is particularly noteworthy is: $O_2^{\bullet-} + H_2O \leftrightharpoons HO_2^{\bullet} + HO^-$. The rapid reaction between superoxide radical and H_2O is well-known.[54,55] Here, we hypothesize that superoxide more rapidly reacts with adsorbed water than methylammonium, shifting the rate determining step, and thus significantly altering the rate equation. One plausible water-mediated photo-oxidation pathway is shown in Scheme 2. (see alternative pathways in §7 of Supporting Information)

Scheme 2. One Plausible Water-Accelerated Photo-oxidation Pathway. Primary degradation mechanism of MAPbI$_3$ in the presence of water, oxygen, above bandgap incident photons, and surface adsorption sites [*].

$$2h\nu \rightarrow 2e^- + 2h^+ \qquad \text{(step 1W)}$$

$$O_2 + [*] \rightleftharpoons O_2^* \qquad \text{(step 2W)}$$

$$O_2^* + e^- \rightleftharpoons O_2^{*\bullet-} \qquad \text{(step 3W)}$$

$$H_2O + [*] \rightleftharpoons H_2O^* \qquad \text{(step 4W)}$$

$$O_2^{\bullet-*} + H_2O^* \rightleftharpoons HO_2^{\bullet*} + HO^{-*} \qquad \text{(step 5W)}$$

$$CH_3NH_3PbI_3 + HO_2^{\bullet*} \rightarrow H_2O_2^* + PbI_2 + CH_3NH_2 + I^{\bullet} \qquad \text{(step 6W)}$$

$$H_2O_2^* + e^- + [*] \rightleftharpoons HO^{-*} + HO^{\bullet*} \qquad \text{(step 7W)}$$

$$CH_3NH_3PbI_3 + HO^{\bullet*} \rightarrow H_2O^* + PbI_2 + CH_3NH_2 + I^{\bullet} \qquad \text{(step 8W)}$$

$$2CH_3NH_3PbI_3 + 2HO^- \rightarrow 2H_2O^* + 2PbI_2 + 2CH_3NH_2 + 2I^- \qquad \text{(step 9W)}$$

$$2h^+ + 2CH_3NH_3PbI_3 \rightleftharpoons 2CH_3NH_3PbI_2^+ + 2[*] + 2I^{\bullet} \qquad \text{(step 10W)}$$

$$2CH_3NH_3PbI_2^+ + 2[*] + 2I^- \rightleftharpoons 2CH_3NH_3PbI_3 \qquad \text{(step 11W)}$$

$$4I^{\bullet} \rightarrow 2I_2 \qquad \text{(step 12W)}$$

Since water is regenerated in this reaction, it has a catalyst-like effect. An expression for the rate of MAPbI$_3$ degradation in humid air is determined by assuming: (i) the rate determining step in Scheme 2 is step 5W—deprotonation of water by superoxide to form hydroxide and hydroperoxyl radicals—and (ii) the fractional surface coverage of water θ_{H_2O} is small in the range of humidity levels studied (i.e. $K_{4W}P_{H_2O} \ll 1 + K_{2W}P_{O_2}(1 + K_{3W}n)$, and we are hence in the quasilinear regime of the Langmuir isotherm of water such that $\theta_{H_2O} \approx K_{4W}P_{H_2O}$).

With these assumptions, r_{WPO} simplifies to (see §7 of Supporting Information for the derivation):

$$r_{WPO} = -k_{WPO} \frac{P_{H_2O}P_{O_2}n}{\left(1 + K_{2W}P_{O_2}(1 + K_{3W}n)\right)^2} \qquad \textbf{(14)}$$

where $k_{WPO} = k_{0,WPO}\, e^{-E_{A,WPO}^{\text{eff}}/k_B T}$. In order to assess the validity of the functional forms of the derived rate equations for DPO and WPO, the measured rate data are plotted as functions of oxygen concentration and photon flux and fitted to Equations 13 & 14 in Figure 4, along with simple power

law relations (the functional forms fit in Figure 3). Figure 4 demonstrates that when varying illumination intensity in air, as well as from varying oxygen content under 1 sun illumination intensity, degradation rates match the functional forms expressed in Equations 13 & 14 as well as or better than simple rate law dependence. These functional forms are summarized for each set of conditions in Table 2.

Some research groups have disputed the commonly held consensus that water is produced as a byproduct in the dry photooxidation reaction.[20,25] They claim instead a mechanism where $2HO_2^{\cdot}$ species react once generated to form $O_2 + H_2$ instead of water vapor. This possibility is explored in §6-7 of Supporting Information. Due to the rate limiting step in both mechanisms being shared—namely, that proton abstraction by superoxide is rate-limiting—both mechanisms yield the same rate expression for r_{DPO} and r_{WPO}. Similarly, presence of excess holes due to photogeneration and subsequent reaction of photoexcited electrons may trigger generation of iodide vacancies in MAPbI$_3$.[44] As iodide vacancies are the primary adsorption sites for both water vapor and oxygen, this can act as a generation reaction of new adsorption sites.[19,44,52] However, due to the mismatch in time scales between vacancy generation from holes and material degradation,[44] as well as the presence of many other adsorption sites for degradation,[52,56] the assumption that total adsorption site density is constant remains valid on these early timescales, leading to the same rate expressions for r_{DPO} and r_{WPO} (see (see §8 of Supporting Information for more details).
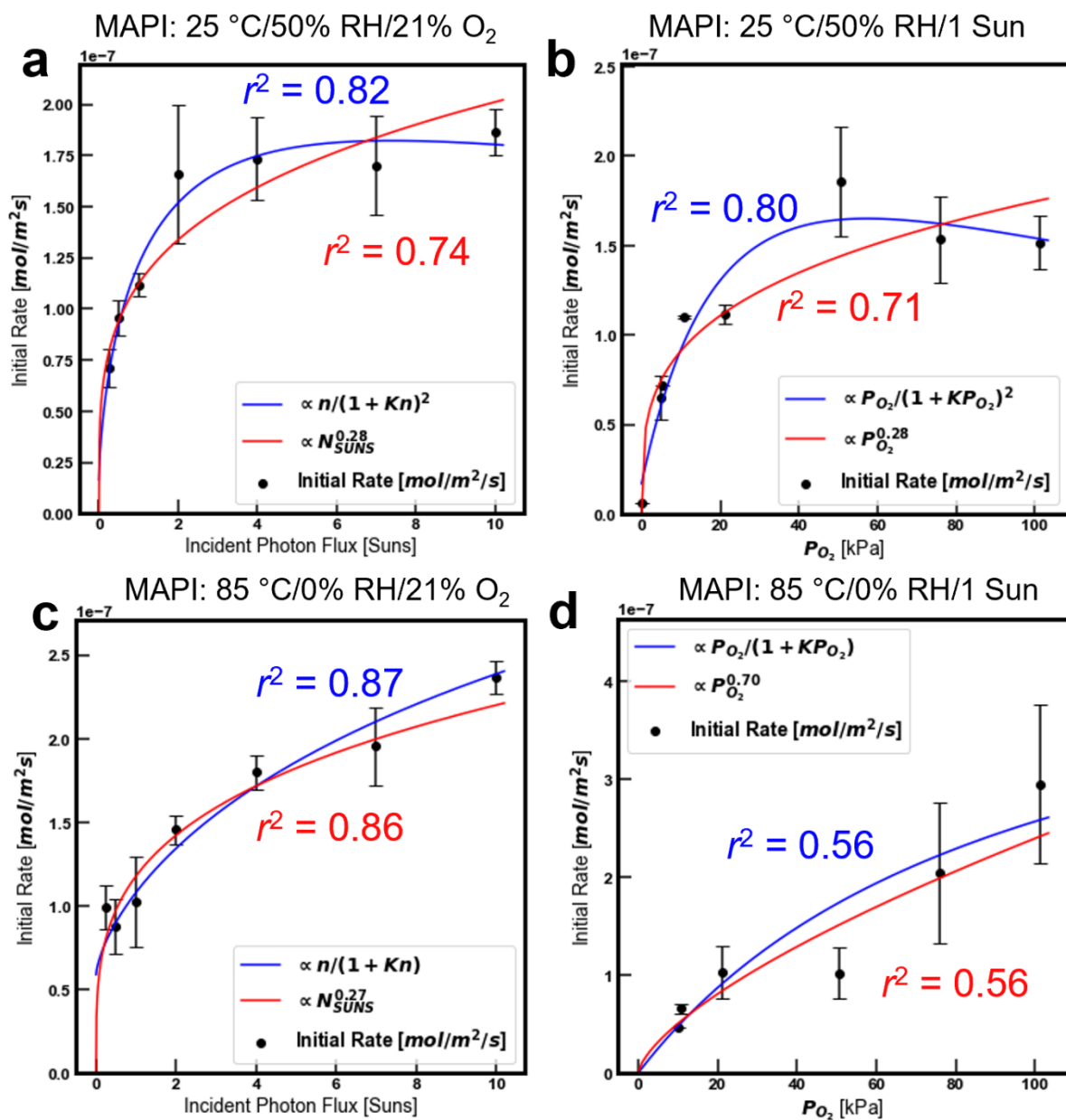
Figure 4. Rate of MAPbI$_3$ degradation vs (a,c) incident photon flux and (b,d) oxygen partial pressure in (a,b) 25 °C air at 50% RH and (c,d) 85 °C air at 0% RH. Note the rate order w.r.t photon intensity is equal to the power law dependence between photon intensity and electron concentration (and consequently the activity of electrons)[43,47] We see that the data for humid air fits the functional forms $n/(1 + Kn)^2$ and $P_{O_2}/\left(1 + KP_{O_2}\right)^2$ that are derived from the mechanism (assuming a rate limiting step) better than simple power laws – the mechanism predicts the turnover at high P_{O_2}. For the data in dry air, the derived expressions $n/(1 + Kn)$ and $P_{O_2}/\left(1 + KP_{O_2}\right)$ fit data equally well as simple power law relations.

Table 2. A summary table of the functional forms of initial rate r_{MAPI} versus oxygen, moisture, and electron concentrations.

$r \propto f(X)$	0% RH	50% RH
$f(P_{O_2})$	$\dfrac{P_{O_2}}{1 + KP_{O_2}}$	$\dfrac{P_{O_2}}{\left(1 + KP_{O_2}\right)^2}$
$f(n)$	$\dfrac{n}{1 + Kn}$	$\dfrac{n}{(1 + Kn)^2}$
$f(P_{H_2O})$	--	P_{H_2O}

Table 3. Fit parameters for the parity plot in Figure 5. Partial pressures of oxygen and moisture are expressed in kPa, temperature in K, and incident above-bandgap-photon-flux I_{in} in photons·m^{-2}·s^{-1}. Boltzmann's constant is expressed as 8.617×10^{-5} eV/K, and $E_{A,WPO}^{\text{eff}}$ and $E_{A,DPO}^{\text{eff}}$ are the effective activation energies for the water-assisted and dry photooxidation pathways. Note that: (i) r_{other} captures the rate from all other degradation pathways (see §10.2 in Supporting Information), (ii) $n \propto I_{in}^{0.7}$, and (iii) $E_{A,WPO}^{\text{eff}} = E_A + \Delta H_{ads,H_2O}$ (see §10.1 in Supporting Information); since adsorption is expected to be exothermic (i.e. $\Delta H_{ads,H_2O} < 0$), the effective activation energy of WPO will be negative if $E_A < |\Delta H_{ads,H_2O}|$.

Equation
$$r = k_{0,WPO} \exp\left(-\frac{E_{A,WPO}^{\text{eff}}}{k_B T}\right) \frac{P_{O_2} P_{H_2O} I_{in}^{0.7}}{\left(1 + K_{2W} P_{O_2}\left(1 + K_{3W} I_{in}^{0.7}\right)\right)^2}$$ $$+ k_{0,DPO} \exp\left(-\frac{E_{A,DPO}^{\text{eff}}}{k_B T}\right) \frac{P_{O_2} I_{in}^{0.7}}{1 + K_{2D} P_{O_2}\left(1 + K_{3D} I_{in}^{0.7}\right)} + r_{other}$$

Parameter	Humid Air (WPO pathway)	Dry Air (DPO pathway)
k_0	$3.16 \times 10^{-25} \dfrac{mol}{m^2\, s\, kPa^2}\left(\dfrac{photons}{m^2 \cdot s}\right)^{-0.7}$	$5.45 \times 10^{-15} \dfrac{mol}{m^2 s\, kPa}\left(\dfrac{photons}{m^2 s}\right)^{-0.7}$
E_A^{eff}	$-0.09\ eV$	$0.62\ eV$
K_2	$4.40 \times 10^{-3}\ kPa^{-1}$	$3.28 \times 10^{-3}\ kPa^{-1}$
K_3	$4.32 \times 10^{-15}\left(\dfrac{photons}{m^2 \cdot s}\right)^{-0.7}$	$6.97 \times 10^{-15}\left(\dfrac{photons}{m^2 \cdot s}\right)^{-0.7}$

Having established the basic mathematical forms of the majority degradation pathways (i.e., WPO and DPO), we construct and fit a model for the net degradation rate $r = r_{DPO} + r_{WPO} + r_{other}$ in arbitrary conditions, where r_{other} represents minority pathways of wet photo-thermal decomposition (without oxygen) and dry photo-thermal decomposition (without moisture or oxygen). The equation and fit parameters corresponding to the WPO and DPO pathways are given in Table 3; the functional form and parameters of r_{other} may be found in §10 of the Supporting Information, as well as details of the fitting procedure. To validate this model, the calculated net degradation rate is compared against observed degradation rates for all runs used to fit the model (95 total runs) in Figure 5a. While there exists sample-to-sample variation of observed degradation rate within a given set of environmental conditions, the model in Table 3 does a good job of predicting the mean degradation rate of MAPbI$_3$ at a given set of environmental conditions, with an r^2 of 0.74 demonstrating good parity between observed and modeled degradation rates. Furthermore, use of the Bootstrap algorithm[57] demonstrates model stability as well. Bootstrap assesses how stable a model is by resampling model training data with replacement for a certain number of iterations (1000 iterations in Figures S21 and S22). Fits of resampled data are then collected and confidence intervals for each of the fit parameters (in Table 3) are determined based on distributions of fit parameters extracted from resampled datasets.[57] Figures S21 and S22 demonstrate that our model predicts tight confidence intervals surrounding fits of WPO and DPO rate expressions after Bootstrap resampling, demonstrating that the modeling task behaves stably and is representative of experimental degradation rates. (See §14 of Supporting Information for more details.) Given the accuracy of the predictive model and the narrow confidence interval of fit parameters, the values of K_2 (~4 x 10^{-3} kPa^{-1}) and K_3 (~5 x 10^{-15} (photons/(m^{2}s))$^{-0.7}$) obtained in this manner provide the first experimental estimate of the equilibrium constants of oxygen adsorption on MAPbI$_3$ surfaces (K_2) and oxygen reduction to superoxide from photoexcited electrons in the conduction band (K_3). The consistency of the values of K_2 and K_3 between dry and humid conditions indicates that the impact of moisture on O$_2$ adsorption and reduction is extremely weak, in general agreement with our experimental results. This behavior is also consistent with our observations of 1st order kinetics with respect to P_{H_2O} and sublinear kinetics with respect to P_{O_2}, which indicate that the surface concentration of water is much less than that of neutral oxygen and is therefore unlikely to have a large impact on the latter prior to its conversion to superoxide. Ultimately, the form of our rate model *and* the calculated values of its parameters suggest that the accelerating effect of water on photooxidation is primarily due to providing a lower-activation energy pathway by which superoxide may react, rather than affecting adsorption or reduction of neutral oxygen.
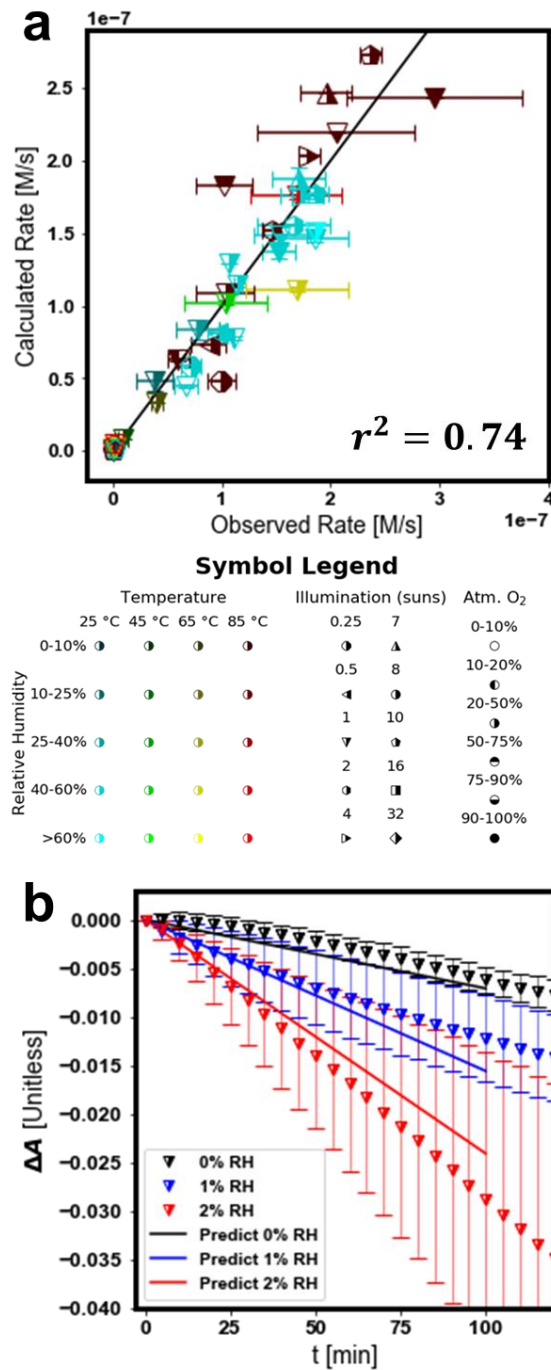
Figure 5. (a) Parity plot comparing observed degradation rate against the sum of the humid and dry photooxidation rate expressions calculated based on rate order data. A good fit is achieved, with an r² of 0.74. (b) WPO rate expressions are able to calculate degradation rates down to ~1% RH, showing even at these low levels of humidity, the WPO rate proceeds significantly faster than DPO alone. Data shown are at 25 °C in air under 1 sun illumination.

The rate expressions in Equations 13 & 14 provide surprising implications for HP stability and accelerated aging of perovskite thin films. Contour plots of the prediction of total degradation rate $r = r_{DPO} + r_{WPO} + r_{other}$ are shown in Figure 6. See §10 of Supporting Information for more detail on how rate was calculated in environmental conditions where multiple degradation pathways are likely to significantly contribute to observed degradation rate (e.g. hot and humid air, very low humidity, etc.).
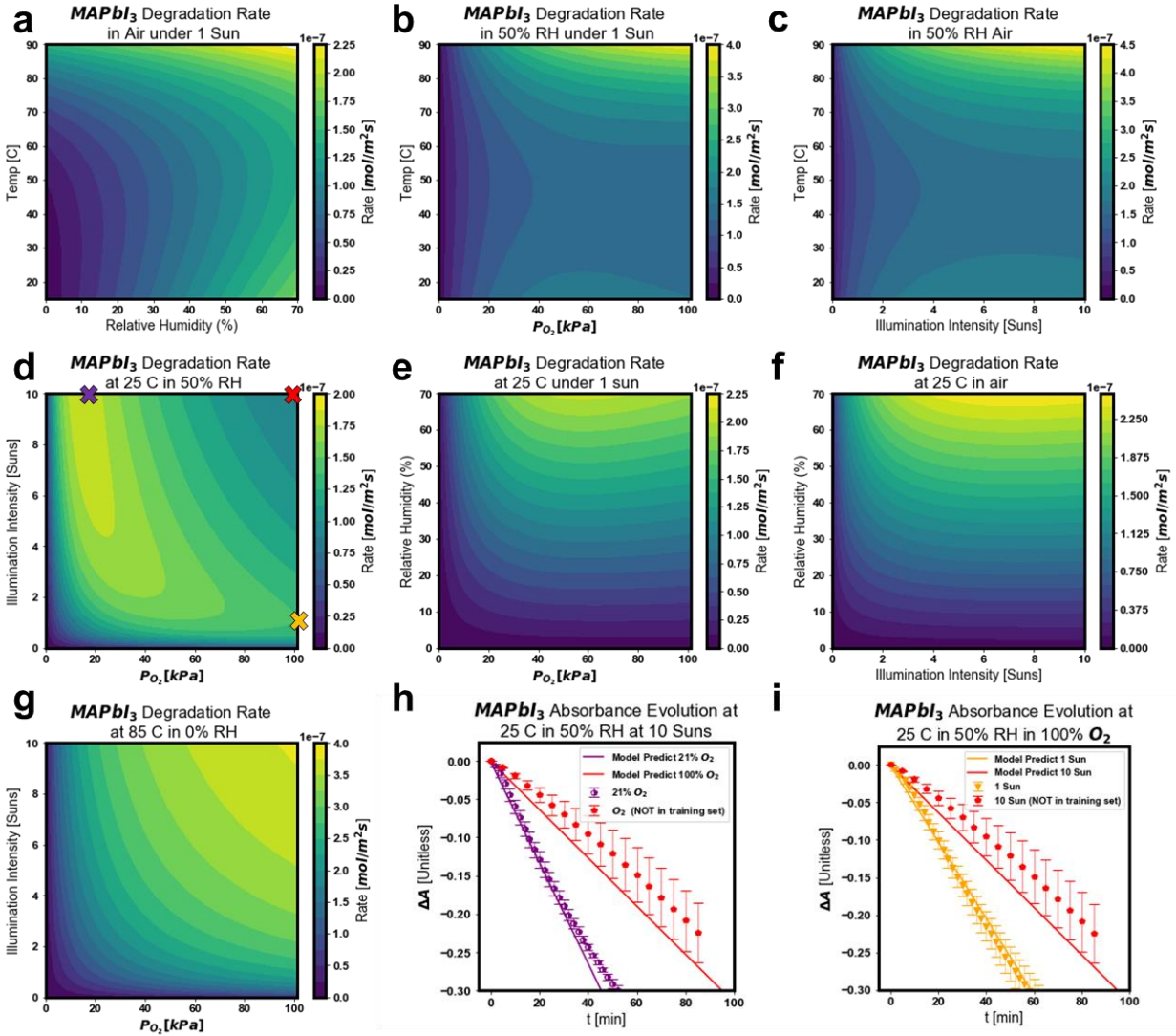
Figure 6. (a-g) Contour maps of $r = r_{DPO} + r_{WPO} + r_{other}$ showing the functionality of the calculated rate expressions. Mechanistic crossover from DPO-dominant to WPO-dominant degradation and calculation of degradation due to minority pathways is accounted for in Supporting Information §10. (h-i) Degradation of MAPbI$_3$ in 10 suns in pure O$_2$, validating the model prediction that humid air degradation occurs more slowly in increasing levels of (h) oxygen and (i) illumination intensity. Note data collected in 10 suns in O$_2$ was not used to fit the model; therefore, this result is validation of the functional form of r_{WPO} in extrapolated environmental conditions. Model predicted rates in (h-i) are taken from model predictions at points in condition space labeled in panel (d).

One especially counter-intuitive conclusion of the functional form of r_{WPO} in Equation 14 is that above critical values, increasing oxygen content and illumination intensity *decreases* degradation rate of MAPbI$_3$ (Figure 6d). To validate this conclusion, MAPbI$_3$ degradation was measured at 25 °C 50% RH O$_2$ under 10 suns illumination intensity. Note that r_{WPO} rate constants and functionalities were calculated from degradation experiments under 1 sun with changing oxygen pressure and in 21% O$_2$ with changing illumination intensity. Therefore, 10 suns in 100% O$_2$ is an extrapolated environmental condition set relative to data used to fit the r_{WPO} equation. Nonetheless, degradation data collected in these conditions confirms the conclusions of the model (Figure 6h-i): degradation rates under high levels of oxygen *and* illumination stress are much slower than degradation rates under high levels of oxygen *or* illumination stress.

The mechanism and functional forms of r_{DPO} and r_{WPO} have significant implications for commercialization of halide perovskite technologies, particularly for stability validation and accelerated aging test protocols. The functional form of the rate law in humidity and resultant decelerating degradation rate indicate that caution should be used in interpreting conventional stability tests. High-temperature accelerated aging tests may be problematic, as degradation at high temperatures (~85 °C) is dominated by the dry-photooxidation pathway, while degradation at 25 °C is dominated by the water accelerated photooxidation process. The contour plots, particularly Figure 6d, suggests that accelerated testing at 6 Suns in humid air at 25 °C may be useful. However, going to high oxygen concentration at any illumination is likely a bad idea since oxygen starts to out compete water for surface adsorption sites, decreasing the overall degradation rate.

Furthermore, results from this work have implications for packaging and encapsulation of halide perovskite optoelectronics. Encapsulation materials—and even in some cases hole transporting materials—are specifically designed for hydrophobicity. However, results of this work demonstrate that oxygen ingress is likely the most important process to inhibit, as it is required for DPO and WPO. Unfortunately, flexible encapsulant layers have traditionally been unable to effectively block oxygen as effectively as moisture. While water-repellent barrier layers may still stabilize perovskites at room-temperature by eliminating the WPO pathway at early times, these water-resistant layers may themselves be problematic. It is widely proposed that water is a byproduct of the photooxidation reaction,[6,19,24] and here we have shown that small amounts of water can dramatically increase perovskite degradation rate by the WPO pathway. The data and model both demonstrate (Figure 5b) that the WPO predominates at 25 °C in air with humidity values as low as ~1% RH (~150 ppm H$_2$O by mass). If water is produced during the photooxidation reaction and then trapped on the perovskite surface by the hydrophobic barrier layer, even tiny amounts of residual water buildup near the halide perovskite surface may set off the water-accelerated photo-oxidation process over longer timescales, decreasing overall stability. This conclusion may help explain recent results demonstrating increased PV stability in perovskites from hydrophilic passivation layers,[58] as these layers may help getter water generated from the photooxidation process away from the perovskite, arresting the water-accelerated photooxidative pathway.

Conclusions

Fundamental kinetics governing the early-time degradation of halide perovskite MAPbI$_3$ were discovered in a unique automated data collection apparatus in a variety of controlled environmental conditions. Using absorbance at 550 nm as a probe of degradation extent, two predominant modes of degradation were identified: (1) photooxidation due solely to the interaction of oxygen and photoexcited electrons (E_{DPO}^{eff} = 0.62 eV), and (2) humidity-accelerated photooxidation (E_{WPO}^{eff} = -0.09 eV). For each of these degradation modes, we identified rate orders with respect to oxygen, humidity, and light intensity using rate constants extracted from linear fits of early-time absorbance evolution. Based on derived rate expressions, we propose a fundamental mechanism that details how oxygen degrades the MAPbI$_3$ lattice, including detail on the catalytic role of moisture in MAPbI$_3$ photooxidation.

Acknowledgments

Legal Disclaimer

Declarations

The authors declare no competing financial interests.

Supporting Information

Experimental details; quantification of absorbance and reflectance as a function of degradation extent; thickness-dependent degradation rate; degradation rates in dark environments; relationship between activity of photoexcited electrons, photoconductivity, and photon flux and illumination intensity vs photoconductivity plot; derivations of rate equations for dry and water-accelerated photooxidation; how convective flow rate of MAPbI$_3$ impacts degradation rate; investigation into the effects of changing adsorption surface site concentration; calculation of

water-accelerated photooxidation as a function of temperature; raw ΔA vs time data and linear fits of all data used in Figures 2-6; characterizing the effects of "pre-anneal" used to dry thin films before limiting case experiments; *J-V* curves of devices made from $MAPbI_3$ films and morphology; estimating sources of measurement error in degradation runs; discussion of the bootstrap algorithm used to quantify uncertainty in model parameter estimation.

References

(1)   Yoo, J. J.; Seo, G.; Chua, M. R.; Park, T. G.; Lu, Y.; Rotermund, F.; Kim, Y.-K.; Moon, C. S.; Jeon, N. J.; Correa-Baena, J.-P.; Bulović, V.; Shin, S. S.; Bawendi, M. G.; Seo, J. Efficient Perovskite Solar Cells via Improved Carrier Management. *Nature* **2021**, *590* (7847), 587–593. https://doi.org/10.1038/s41586-021-03285-w.

(2)   Chang, N. L.; Ho-Baillie, A. W. Y.; Vak, D.; Gao, M.; Green, M. A.; Egan, R. J. Manufacturing Cost and Market Potential Analysis of Demonstrated Roll-to-Roll Perovskite Photovoltaic Cell Processes. *Sol. Energy Mater. Sol. Cells* **2018**, *174*, 314–324. https://doi.org/10.1016/j.solmat.2017.08.038.

(3)   Mathews, I.; Sofia, S.; Ma, E.; Jean, J.; Laine, H. S.; Siah, S. C.; Buonassisi, T.; Peters, I. M. Economically Sustainable Growth of Perovskite Photovoltaics Manufacturing. *Joule* **2020**, *4* (4), 822–839. https://doi.org/10.1016/j.joule.2020.01.006.

(4)   Mazzarella, L.; Lin, Y.; Kirner, S.; Morales-Vilches, A. B.; Korte, L.; Albrecht, S.; Crossland, E.; Stannowski, B.; Case, C.; Snaith, H. J.; Schlatmann, R. Infrared Light Management Using a Nanocrystalline Silicon Oxide Interlayer in Monolithic Perovskite/Silicon Heterojunction Tandem Solar Cells with Efficiency above 25%. *Adv. Energy Mater.* **2019**, *9* (14), 1803241. https://doi.org/10.1002/aenm.201803241.

(5)   Al-Ashouri, A.; Köhnen, E.; Li, B.; Magomedov, A.; Hempel, H.; Caprioglio, P.; Márquez, J. A.; Morales Vilches, A. B.; Kasparavicius, E.; Smith, J. A.; Phung, N.; Menzel, D.; Grischek, M.; Kegelmann, L.; Skroblin, D.; Gollwitzer, C.; Malinauskas, T.; Jošt, M.; Matič, G.; Rech, B.; Schlatmann, R.; Topič, M.; Korte, L.; Abate, A.; Stannowski, B.; Neher, D.; Stolterfoht, M.; Unold, T.; Getautis, V.; Albrecht, S. Monolithic Perovskite/Silicon Tandem Solar Cell with >29% Efficiency by Enhanced Hole Extraction. *Science* **2020**, *370* (6522), 1300–1309. https://doi.org/10.1126/science.abd4016.

(6)   Dunfield, S. P.; Bliss, L.; Zhang, F.; Luther, J. M.; Zhu, K.; Hest, M. F. A. M.; Reese, M. O.; Berry, J. J. From Defects to Degradation: A Mechanistic Understanding of Degradation in Perovskite Solar Cell Devices and Modules. *Adv. Energy Mater.* **2020**, *10* (26), 1904054. https://doi.org/10.1002/aenm.201904054.

(7)   Matsui, T.; Yamamoto, T.; Nishihara, T.; Morisawa, R.; Yokoyama, T.; Sekiguchi, T.; Negami, T. Compositional Engineering for Thermally Stable, Highly Efficient Perovskite Solar Cells Exceeding 20% Power Conversion Efficiency with 85 °C/85% 1000 h Stability. *Adv. Mater.* **2019**, *31* (10), 1806823. https://doi.org/10.1002/adma.201806823.

(8)   Shi, L.; Bucknall, M. P.; Young, T. L.; Zhang, M.; Hu, L.; Bing, J.; Lee, D. S.; Kim, J.; Wu, T.; Takamure, N.; McKenzie, D. R.; Huang, S.; Green, M. A.; Ho-Baillie, A. W. Y. Gas Chromatography–Mass Spectrometry Analyses of Encapsulated Stable Perovskite Solar Cells. *Science* **2020**, *368* (6497), eaba2412. https://doi.org/10.1126/science.aba2412.

(9)   Choi, K.; Lee, J.; Choi, H.; Kim, G.-W.; Kim, H. I.; Park, T. Heat Dissipation Effects on the Stability of Planar Perovskite Solar Cells. *Energy Environ. Sci.* **2020**, *13* (12), 5059–5067. https://doi.org/10.1039/D0EE02859B.

(10)   Yang, N.; Zhu, C.; Chen, Y.; Zai, H.; Wang, C.; Wang, X.; Wang, H.; Ma, S.; Gao, Z.; Wang, X.; Hong, J.; Bai, Y.; Zhou, H.; Cui, B.-B.; Chen, Q. An *in Situ* Cross-Linked 1D/3D Perovskite

Heterostructure Improves the Stability of Hybrid Perovskite Solar Cells for over 3000 h Operation. *Energy Environ. Sci.* **2020**, *13* (11), 4344–4352. https://doi.org/10.1039/D0EE01736A.

(11)   US Department of Energy Solar Energy Technologies Office. *The Sunshot 2030 Goals: 3 Cent per Kilowatt Hour for PV and 5 Cent per Kilowatt Hour for Dispatchable CSP*; White Paper DOE/EE-1501; US Department of Energy, Office of Energy Efficiency and Renewable Energy, 2017.

(12)   International Electrotechnical Commission. *IEC 61215-2:2021 RLV Redline Version. Terrestrial Photovoltaic Modules-Design Qualification and Type Approval*; Testing Standards IEC 61215-2:2021; International Electrotechnical Commission: Geneva, Switzerland, 2021.

(13)   Jordan, D. C.; Kurtz, S. R. Photovoltaic Degradation Rates-an Analytical Review: Photovoltaic Degradation Rates. *Prog. Photovolt. Res. Appl.* **2013**, *21* (1), 12–29. https://doi.org/10.1002/pip.1182.

(14)   Lindroos, J.; Savin, H. Review of Light-Induced Degradation in Crystalline Silicon Solar Cells. *Sol. Energy Mater. Sol. Cells* **2016**, *147*, 115–126. https://doi.org/10.1016/j.solmat.2015.11.047.

(15)   Gretener, C.; Perrenoud, J.; Kranz, L.; Cheah, E.; Dietrich, M.; Buecheler, S.; Tiwari, A. N. New Perspective on the Performance Stability of CdTe Solar Cells. *Sol. Energy Mater. Sol. Cells* **2016**, *146*, 51–57. https://doi.org/10.1016/j.solmat.2015.11.017.

(16)   Christians, J. A.; Miranda Herrera, P. A.; Kamat, P. V. Transformation of the Excited State and Photovoltaic Efficiency of $CH_3NH_3PbI_3$ Perovskite upon Controlled Exposure to Humidified Air. *J. Am. Chem. Soc.* **2015**, *137* (4), 1530–1538. https://doi.org/10.1021/ja511132a.

(17)   Müller, C.; Glaser, T.; Plogmeyer, M.; Sendner, M.; Döring, S.; Bakulin, A. A.; Brzuska, C.; Scheer, R.; Pshenichnikov, M. S.; Kowalsky, W.; Pucci, A.; Lovrinčić, R. Water Infiltration in Methylammonium Lead Iodide Perovskite: Fast and Inconspicuous. *Chem. Mater.* **2015**, *27* (22), 7835–7841. https://doi.org/10.1021/acs.chemmater.5b03883.

(18)   Wei, J.; Wang, Q.; Huo, J.; Gao, F.; Gan, Z.; Zhao, Q.; Li, H. Mechanisms and Suppression of Photoinduced Degradation in Perovskite Solar Cells. *Adv. Energy Mater.* **2021**, *11* (3), 2002326. https://doi.org/10.1002/aenm.202002326.

(19)   Aristidou, N.; Sanchez-Molina, I.; Chotchuangchutchaval, T.; Brown, M.; Martinez, L.; Rath, T.; Haque, S. A. The Role of Oxygen in the Degradation of Methylammonium Lead Trihalide Perovskite Photoactive Layers. *Angew. Chem.* **2015**, *127* (28), 8326–8330. https://doi.org/10.1002/ange.201503153.

(20)   Nickel, N. H.; Lang, F.; Brus, V. V.; Shargaieva, O.; Rappich, J. Unraveling the Light-Induced Degradation Mechanisms of $CH_3NH_3PbI_3$ Perovskite Films. *Adv. Electron. Mater.* **2017**, *3* (12), 1700158. https://doi.org/10.1002/aelm.201700158.

(21)   Stoddard, R. J.; Dunlap-Shohl, W. A.; Qiao, H.; Meng, Y.; Kau, W. F.; Hillhouse, H. W. Forecasting the Decay of Hybrid Perovskite Performance Using Optical Transmittance or Reflected Dark-Field Imaging. *ACS Energy Lett.* **2020**, *5* (3), 946–954. https://doi.org/10.1021/acsenergylett.0c00164.

(22)   Lin, H.-J.; Cacovich, S.; Rebai, A.; Rousset, J.; Longeaud, C. Influence of Environment and Light-Stress on the Optoelectronic Properties of Triple-Cation Perovskite Thin Films. *ACS Appl. Mater. Interfaces* **2020**, *12* (17), 19495–19503. https://doi.org/10.1021/acsami.0c01732.

(23)   Aristidou, N.; Eames, C.; Islam, M. S.; Haque, S. A. Insights into the Increased Degradation Rate of $CH_3NH_3PbI_3$ Solar Cells in Combined Water and O_2 Environments. *J. Mater. Chem. A* **2017**, *5* (48), 25469–25475. https://doi.org/10.1039/C7TA06841G.

(24)   Aristidou, N.; Eames, C.; Sanchez-Molina, I.; Bu, X.; Kosco, J.; Islam, M. S.; Haque, S. A. Fast Oxygen Diffusion and Iodide Defects Mediate Oxygen-Induced Degradation of Perovskite Solar Cells. *Nat. Commun.* **2017**, *8* (1), 15218. https://doi.org/10.1038/ncomms15218.

(25)   Rappich, J.; Lang, F.; Brus, V. V.; Shargaieva, O.; Dittrich, T.; Nickel, N. H. Light-Induced Defect Generation in $CH_3NH_3PbI_3$ Thin Films and Single Crystals. *Sol. RRL* **2020**, *4* (2), 1900216. https://doi.org/10.1002/solr.201900216.

(26)   Sun, S.; Tiihonen, A.; Oviedo, F.; Liu, Z.; Thapa, J.; Zhao, Y.; Hartono, N. T. P.; Goyal, A.; Heumueller, T.; Batali, C.; Encinas, A.; Yoo, J. J.; Li, R.; Ren, Z.; Peters, I. M.; Brabec, C. J.; Bawendi, M. G.; Stevanovic, V.; Fisher, J. I.; Buonassisi, T. A Data Fusion Approach to Optimize

Compositional Stability of Halide Perovskites. *Matter* **2021**, *4* (4), 1305–1322. https://doi.org/10.1016/j.matt.2021.01.008.

(27) Higgins, K.; Valleti, S. M.; Ziatdinov, M.; Kalinin, S. V.; Ahmadi, M. Chemical Robotics Enabled Exploration of Stability in Multicomponent Lead Halide Perovskites via Machine Learning. *ACS Energy Lett.* **2020**, *5* (11), 3426–3436. https://doi.org/10.1021/acsenergylett.0c01749.

(28) Hartono, N. T. P.; Thapa, J.; Tiihonen, A.; Oviedo, F.; Batali, C.; Yoo, J. J.; Liu, Z.; Li, R.; Marrón, D. F.; Bawendi, M. G.; Buonassisi, T.; Sun, S. How Machine Learning Can Help Select Capping Layers to Suppress Perovskite Degradation. *Nat. Commun.* **2020**, *11* (1), 4172. https://doi.org/10.1038/s41467-020-17945-4.

(29) Stutzmann, M.; Jackson, W. B.; Tsai, C. C. Kinetics of the Staebler–Wronski Effect in Hydrogenated Amorphous Silicon. *Appl. Phys. Lett.* **1984**, *45* (10), 1075–1077. https://doi.org/10.1063/1.95020.

(30) Akbulatov, A. F.; Ustinova, M. I.; Shilov, G. V.; Dremova, N. N.; Zhidkov, I. S.; Kurmaev, E. Z.; Frolova, L. A.; Shestakov, A. F.; Aldoshin, S. M.; Troshin, P. A. Temperature Dynamics of MAPbI$_3$ and PbI$_2$ Photolysis: Revealing the Interplay between Light and Heat, Two Enemies of Perovskite Photovoltaics. *J. Phys. Chem. Lett.* **2021**, *12* (18), 4362–4367. https://doi.org/10.1021/acs.jpclett.1c00883.

(31) Avrami, M. Kinetics of Phase Change. I General Theory. *J. Chem. Phys.* **1939**, *7* (12), 1103–1112. https://doi.org/10.1063/1.1750380.

(32) Siegler, T. D.; Houck, D. W.; Cho, S. H.; Milliron, D. J.; Korgel, B. A. Bismuth Enhances the Stability of CH$_3$NH$_3$PbI$_3$ (MAPI) Perovskite under High Humidity. *J. Phys. Chem. C* **2019**, *123* (1), 963–970. https://doi.org/10.1021/acs.jpcc.8b11674.

(33) Ellis, C. L. C.; Javaid, H.; Smith, E. C.; Venkataraman, D. Hybrid Perovskites with Larger Organic Cations Reveal Autocatalytic Degradation Kinetics and Increased Stability under Light. *Inorg. Chem.* **2020**, *59* (17), 12176–12186. https://doi.org/10.1021/acs.inorgchem.0c01133.

(34) Charles, B.; Dillon, J.; Weber, O. J.; Islam, M. S.; Weller, M. T. Understanding the Stability of Mixed A-Cation Lead Iodide Perovskites. *J. Mater. Chem. A* **2017**, *5* (43), 22495–22499. https://doi.org/10.1039/C7TA08617B.

(35) Pool, V. L.; Dou, B.; Van Campen, D. G.; Klein-Stockert, T. R.; Barnes, F. S.; Shaheen, S. E.; Ahmad, M. I.; van Hest, M. F. A. M.; Toney, M. F. Thermal Engineering of FAPbI3 Perovskite Material via Radiative Thermal Annealing and in Situ XRD. *Nat. Commun.* **2017**, *8* (1), 14075. https://doi.org/10.1038/ncomms14075.

(36) Meng, K.; Wang, X.; Li, Z.; Liu, Z.; Qiao, Z.; Wang, C.; Hu, Y.; Li, S.; Cheng, L.; Zhai, Y.; Chen, G. Self-Passivation of Low-Dimensional Hybrid Halide Perovskites Guided by Structural Characteristics and Degradation Kinetics. *Energy Environ. Sci.* **2021**, 10.1039.D0EE03836A. https://doi.org/10.1039/D0EE03836A.

(37) Donakowski, A.; Miller, D. W.; Anderson, N. C.; Ruth, A.; Sanehira, E. M.; Berry, J. J.; Irwin, M. D.; Rockett, A.; Steirer, K. X. Improving Photostability of Cesium-Doped Formamidinium Lead Triiodide Perovskite. *ACS Energy Lett.* **2021**, *6* (2), 574–580. https://doi.org/10.1021/acsenergylett.0c02339.

(38) Ho, K.; Wei, M.; Sargent, E. H.; Walker, G. C. Grain Transformation and Degradation Mechanism of Formamidinium and Cesium Lead Iodide Perovskite under Humidity and Light. *ACS Energy Lett.* **2021**, *6* (3), 934–940. https://doi.org/10.1021/acsenergylett.0c02247.

(39) Lin; Guo; Dai; Lin; Hsu. PbI2 Single Crystal Growth and Its Optical Property Study. *Crystals* **2019**, *9* (11), 589. https://doi.org/10.3390/cryst9110589.

(40) Koutselas, I. B.; Ducasse, L.; Papavassiliou, G. C. Electronic Properties of Three- and Low-Dimensional Semiconducting Materials with Pb Halide and Sn Halide Units. *J Phys Condens Matter* **1996**, *8*, 1217–1227.

(41) Ouyang, Y.; Li, Y.; Zhu, P.; Li, Q.; Gao, Y.; Tong, J.; Shi, L.; Zhou, Q.; Ling, C.; Chen, Q.; Deng, Z.; Tan, H.; Deng, W.; Wang, J. Photo-Oxidative Degradation of Methylammonium Lead Iodide Perovskite: Mechanism and Protection. *J. Mater. Chem. A* **2019**, *7* (5), 2275–2282. https://doi.org/10.1039/C8TA12193A.

(42) Zhao, Y.; Zhang, J.; Xu, Z.; Sun, S.; Langner, S.; Hartono, N. T. P.; Heumueller, T.; Hou, Y.; Elia, J.; Li, N.; Matt, G. J.; Du, X.; Meng, W.; Osvet, A.; Zhang, K.; Stubhan, T.; Feng, Y.; Hauch, J.; Sargent, E. H.; Buonassisi, T.; Brabec, C. J. Discovery of Temperature-Induced Stability Reversal in Perovskites Using High-Throughput Robotic Learning. *Nat. Commun.* **2021**, *12* (1), 2191. https://doi.org/10.1038/s41467-021-22472-x.

(43) Stoddard, R. J.; Eickemeyer, F. T.; Katahara, J. K.; Hillhouse, H. W. Correlation between Photoluminescence and Carrier Transport and a Simple In Situ Passivation Method for High-Bandgap Hybrid Perovskites. *J. Phys. Chem. Lett.* **2017**, *8* (14), 3289–3298. https://doi.org/10.1021/acs.jpclett.7b01185.

(44) Kim, G. Y.; Senocrate, A.; Yang, T.-Y.; Gregori, G.; Grätzel, M.; Maier, J. Large Tunable Photoeffect on Ion Conduction in Halide Perovskites and Implications for Photodecomposition. *Nat. Mater.* **2018**, *17* (5), 445–449. https://doi.org/10.1038/s41563-018-0038-0.

(45) Conings, B.; Drijkoningen, J.; Gauquelin, N.; Babayigit, A.; D'Haen, J.; D'Olieslaeger, L.; Ethirajan, A.; Verbeeck, J.; Manca, J.; Mosconi, E.; Angelis, F. D.; Boyen, H.-G. Intrinsic Thermal Instability of Methylammonium Lead Trihalide Perovskite. *Adv. Energy Mater.* **2015**, *5* (15), 1500477. https://doi.org/10.1002/aenm.201500477.

(46) Singh, A. N.; Kajal, S.; Kim, J.; Jana, A.; Kim, J. Y.; Kim, K. S. Interface Engineering Driven Stabilization of Halide Perovskites against Moisture, Heat, and Light for Optoelectronic Applications. *Adv. Energy Mater.* **2020**, *10* (30), 2000768. https://doi.org/10.1002/aenm.202000768.

(47) Levine, I.; Gupta, S.; Brenner, T. M.; Azulay, D.; Millo, O.; Hodes, G.; Cahen, D.; Balberg, I. Mobility–Lifetime Products in MAPbI $_3$ Films. *J. Phys. Chem. Lett.* **2016**, *7* (24), 5219–5226. https://doi.org/10.1021/acs.jpclett.6b02287.

(48) Boudart, M.; Tamaru, K. The Step That Determines the Rate of a Single Catalytic Cycle. *Catal. Lett.* **1992**, *9*, 15–22. https://doi.org/10.1007/BF00769076.

(49) Kozuch, S.; Martin, J. M. L. The Rate-Determining Step Is Dead. Long Live the Rate-Determining State! *ChemPhysChem* **2011**, *12* (8), 1413–1418. https://doi.org/10.1002/cphc.201100137.

(50) Folger, H. S. *Essentials of Chemical Reaction Engineering*; Pearson College Division, 2010.

(51) Steinfeld, J. I.; Francisco, J. S.; Hase, W. L. *Chemical Kinetics and Dynamics*; Prentice Hall: Upper Saddle River, NJ, USA, 1998.

(52) Ouyang, Y.; Shi, L.; Li, Q.; Wang, J. Role of Water and Defects in Photo-Oxidative Degradation of Methylammonium Lead Iodide Perovskite. *Small Methods* **2019**, *3* (7), 1900154. https://doi.org/10.1002/smtd.201900154.

(53) Godding, J. S. W.; Ramadan, A. J.; Lin, Y.-H.; Schutt, K.; Snaith, H. J.; Wenger, B. Oxidative Passivation of Metal Halide Perovskites. *Joule* **2019**, *3* (11), 2716–2731. https://doi.org/10.1016/j.joule.2019.08.006.

(54) Chin, D. H.; Chiericato, G.; Nanni, E. J.; Sawyer, D. T. Proton-Induced Disproportionation of Superoxide Ion in Aprotic Media. *J. Am. Chem. Soc.* **1982**, *104* (5), 1296–1299. https://doi.org/10.1021/ja00369a025.

(55) Cotton, F. A.; Wilkinson, G. *Basic Inorganic Chemistry*, 1st ed.; John Wiley & Sons, Inc: United States, 1976.

(56) Li, Q.; Chen, Z.; Tranca, I.; Gaastra-Nedea, S.; Smeulders, D.; Tao, S. Compositional Effect on Water Adsorption on Metal Halide Perovskites. *Appl. Surf. Sci.* **2021**, *538*, 148058. https://doi.org/10.1016/j.apsusc.2020.148058.

(57) Efron, B. Bootstrap Methods: Another Look at the Jackknife. In *Breakthroughs in Statistics*; Springer: New York, NY, 1992; pp 569–593.

(58) Ma, C.; Park, N.-G. Paradoxical Approach with a Hydrophilic Passivation Layer for Moisture-Stable, 23% Efficient Perovskite Solar Cells. *ACS Energy Lett.* **2020**, *5* (10), 3268–3275. https://doi.org/10.1021/acsenergylett.0c01848.